Thin Solid Films 519 (2011) 5831–5837

Contents lists available at ScienceDirect

Thin Solid Films

journal homepage: www.elsevier.com/locate/tsf

Annealing effects on microstructure and mechanical properties of sputtered multilayer $Cr_{(1-x)}Al_xN$ films

Xiaolu Pang [a], Huisheng Yang [a,*], Xuelian Liu [a], Kewei Gao [a], Yanbin Wang [a], Alex A. Volinsky [b], Alexandr A. Levin [c]

[a] Department of Materials Physics and Chemistry, University of Science and Technology Beijing, Beijing 100083, China
[b] Department of Mechanical Engineering, University of South Florida, Tampa, FL 33620, USA
[c] Institut für Strukturphysik, Technische Universität Dresden, 01062 Dresden, Germany

ARTICLE INFO

Article history:
Received 5 April 2010
Received in revised form 19 February 2011
Accepted 22 February 2011
Available online 2 March 2011

Keywords:
$Cr_{(1-x)}Al_xN$ films
Microstructure
Annealing
X-ray diffraction
Mechanical properties

ABSTRACT

Multilayer $Cr_{(1-x)}Al_xN$ films with a total thickness of 2 μm were deposited on high-speed steel by medium frequency magnetron sputtering from Cr and Al–Cr (70 at.% Al) targets. The samples were annealed in air at 400 °C, 600 °C, 800 °C and 1000 °C for 1 hour. Films were characterized by cross-sectional scanning electron microscopy and X-ray diffraction analysis. The grain size of the as-deposited multilayer films is about 10 nm, increasing with the annealing temperature up to 100 nm. Interfacial reactions have clearly changed at elevated annealing temperatures. As-deposited films' hardness measured by nanoindentation is 22.6 GPa, which increases to 26.7 GPa when the annealing temperature goes up to 400 and 600 °C, but hardness decreases to 21.2 GPa with further annealing temperature increase from 600 to 1000 °C. The multilayer film adhesion was measured by means of the scratch test combined with acoustic emission for detecting the fracture load. The critical normal load decreased from 49.7 N for the as-deposited films to 21.2 N for the films annealed at 1000 °C.

© 2011 Elsevier B.V. All rights reserved.

1. Introduction

$Cr_{(1-x)}Al_xN$ films have high hardness, high wear, corrosion and oxidation resistance, and good thermal stability, so they have attracted many researchers [1–4]. Recently titanium-based coatings were replaced with $Cr_{(1-x)}Al_xN$ layers because of their higher thermal stability and hardness, particularly in intermediate and high-speed cutting applications [5]. It has been shown that the oxidation behavior of $Cr_{(1-x)}Al_xN$ films is superior to that of $Ti_{(1-x)}Al_xN$ [2]. It is known that materials performance depends on their microstructure and chemical composition, especially for thin films and coatings. Several studies showed that the Al/Cr ratio difference results in the $Cr_{(1-x)}Al_xN$ films microstructure change [5–8]. Fox-Rabinovich et al. [9] argued that the Al content in the $Cr_{(1-x)}Al_xN$ coatings is limited to $x = 0.6–0.7$ range due to the undesirable transformation from B1 (cubic) to B4 (hexagonal) phase in the coatings with higher Al content. Reiter et al. [10] studied mechanical properties of $Cr_{(1-x)}Al_xN$ in relation to the formation and content of the cubic B1 phase. The authors found that the hardness and oxidation resistance were optimal when the aluminum content in $Cr_{(1-x)}Al_xN$ coatings was around $x = 0.7$. Metallic Al–Cr alloy target (Al/Cr at. % ratio = 70:30) was utilized to prepare $Cr_{(1-x)}Al_xN$ coatings in this paper.

One of the important features of the new generation hard protective coatings is high abrasion and oxidation resistance at high temperatures, which plays a key role in increasing the tool lifetime in high-temperature applications. Unfortunately, limited studies focused on the influence of temperature on $Cr_{(1-x)}Al_xN$ coating properties, especially on multilayer $Cr_{(1-x)}Al_xN$ coatings with varying nitrogen content, which is the focus of this paper. Due to thermal expansion coefficients mismatch between the layers and the substrate, higher deposition temperature results in elevated residual stress, which can be relieved by coating fracture and/or delamination, degrading tool performance and reliability.

Based on different applications, various techniques have been used to deposit $Cr_{(1-x)}Al_xN$ films, including sputtering, cathodic arc ion implantation, reactive arc evaporation, plasma physical vapor deposition, reactive cathodic arc processes, etc. [4,10–16]. Various deposition methods result in different films microstructure, which controls their properties, so it is important to know the microstructure of specimens prepared by different deposition techniques. Medium frequency magnetron sputtering has become the process of choice for depositing a wide range of industrially important coatings. Examples include hard, wear-resistant, low friction, corrosion resistant, decorative coatings and coatings with special optical or electrical properties.

In this paper X-ray diffraction (XRD), scanning electron microscopy (SEM), nanoindentation and scratch test techniques were used to characterize annealing effects on the microstructure, phase transformations and mechanical properties of multilayer $Cr_{(1-x)}Al_xN$ films

* Corresponding author.
E-mail address: pangxl@mater.ustb.edu.cn (H. Yang).

0040-6090/$ – see front matter © 2011 Elsevier B.V. All rights reserved.
doi:10.1016/j.tsf.2011.02.063

prepared by medium frequency magnetron sputtering technique. Interfacial reactions and diffusion are also discussed in this paper.

2. Experimental details

$Cr_{(1-x)}Al_xN$ films were deposited on high-speed steel (HSS), $W_{18}Cr_4V$, substrates by medium frequency (20 kHz) magnetron sputtering using metallic Cr and Al–Cr alloy (70 at.% Al) targets with 99.9% purity. The deposition apparatus is shown schematically in Fig. 1(a). Cr target was used to deposit Cr interlayer between the substrate and the multilayer film to improve adhesion. The Al-Cr target was employed to deposit the main layers. An Ar ion source was utilized to enhance the ion intensity, which improves the adhesion and density of coatings. A heater was used to control the chamber temperature, which reached 200 °C during deposition of the 2 μm multilayer films. The rotation rate of the substrate holder was 30 rpm. The target current was 1 A, the base pressure was 2×10^{-4} Pa, and the flow rate of Ar with a purity of 99.99% was 180 sccm. The reactive N_2 gas with 99.99% purity was used, and its flow rate was varied to deposit different layers (Table 1, Fig. 1(b)). The working pressure was 0.5 Pa during film deposition.

Before deposition, the substrates were cleaned in acetone and ethanol for 10 min, respectively, and then subjected to 15 min in-situ Ar plasma cleaning at RF power of 100 W in order to remove any contaminants on the substrate surface and to activate the surface. Chromium interlayer was deposited on the substrates for a duration of 5 min with a DC current of 1 A. Afterwards, N_2 gas was introduced into the reaction chamber with the flow rate ramped from 0 to 3 sccm in 5 min, and kept at 3 sccm for additional 5 min. The substrate temperature was held at 473 K prior to deposition. The total deposition time for 2 μm thick $Cr_{(1-x)}Al_xN$ multilayer with 6 periods and 12 layers was 2 hours based on the deposition parameters shown in Table 1.

After deposition, the samples were annealed in air at 400 °C, 600 °C, 800 °C and 1000 °C, respectively, for 1 h. The microstructure of $Cr_{(1-x)}Al_xN$ films was analyzed by XRD and SEM. The coating atomic structure was examined using Rigaku D/max-RB X-ray powder diffractometer (Bragg–Brentano geometry) with a Cu source ($\lambda_{Cu\text{-}K\alpha}=1.54184$ Å) at X-ray tube 40 kV voltage and 150 mA current. The scanning range of the diffraction angle 2θ was varied from 10° to 90° at 0.02° step size, and a scanning speed of 8°/min by using symmetrically coupled ω-2θ scan mode ($\omega=2\theta/2$ is an angle of incidence X-rays). Additionally, the XRD patterns were recorded in glancing incidence 2θ scan mode where ω was fixed at selected small values between 2° and 6°. The XRD reflection parameters (i.e. Bragg angle $2\theta_{Bragg}$, full width at half maximum (FWHM), maximum I_{max} and integral $I_{integral}$ intensities) were obtained from measured XRD patterns by means of program ANALYZE [17]. Powder Diffraction File-2 (PDF-2) database [18] coupled with Inorganic Crystal Structure Database (ICSD) [19] was used to analyze the crystalline phase content of the samples.

The hardness and Young's modulus of the coatings were characterized using Hysitron Triboindenter with a Berkovich diamond indenter tip. The indenter tip was loaded at a constant rate of 150 μN/s to the maximum load of 3 mN. Hardness and modulus values presented are an average of ten or more indents for each test condition.

Adhesion between films and steel substrates was evaluated as a function of different annealing conditions by means of a scratch test using UMT tribometer. The normal load was continuously increased at a rate of 1 N/s, while the conical diamond tip (120° angle, 200 μm tip radius) was moving at a constant velocity of 0.05 mm/s.

Table 1
$Cr_{(1-x)}Al_xN$ multilayer coating deposition parameters, duration of N_2 flow T_1 and T_2 with rates H_1 and H_2, respectively.

T_1 (s)	T_2 (s)	H_1 (sccm)	H_2 (sccm)	Graphical representation of the N_2 flow rate
600	600	3	2	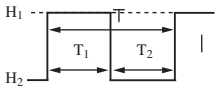

3. Results and discussion

Fig. 2 shows XRD patterns obtained in θ–2θ scan from 2 μm multilayer $Cr_{(1-x)}Al_xN$ films annealed at different temperatures T_{ann}. It can be seen from the XRD patterns that the annealing temperature strongly affects the structure of $Cr_{(1-x)}Al_xN$ films. There are no detectable diffraction reflections in the as-deposited and the 400 °C annealed films, except HSS substrate diffraction reflections and an amorphous hallo contribution in the 30° to 51° 2θ range. With the annealing temperature increasing to 600 °C, the formation of crystalline phases is observed resulting in appearance of separate weak and broaden non-substrate XRD reflections, 0002 reflection of the hexagonal close-packed (hcp) AlN phase [20] and overlapped $11\bar{2}1$ and 200 reflections of hcp Cr_2N [21] and cubic CrN [22], respectively. When T_{ann} increased up to 800 °C, the $11\bar{2}1$ Cr_2N and 200 CrN reflections became resolved and a lot of new weak-intensity XRD reflections of AlN, Cr_2N and CrN crystalline phases were formed. Further increase of the annealing temperature up to 1000 °C results in much stronger intensities of the observed reflections evidencing an increase of the scattering volume of the crystalline phases formed.

After annealing at 1000 °C the new diffraction reflections of body-centered cubic (bcc) Cr [23] were detected, which implies bcc-Cr formation via Cr_2N under N_2 release. Reiter et al. [10], Willmann et al. [6] and Ref. [24] also found that the Cr_2N decomposition resulted in bcc-Cr formation at high annealing temperatures. Additionally, starting from $T_{ann}=800$ °C, many weak-intensity reflections are formed in XRD patterns which can be attributed to monoclinic Al_2O_3 phase [25] formed probably due to the sample oxidation during the high-temperature annealing in air.

The weak intensity and broad profile of the XRD reflections observed after annealing at 600 °C could be caused by formation of small-size crystallites of a crystalline phase from the amorphous phase. The small size of the incoherently diffracting crystallites could be governed by the presence of dislocation arrays, stacking faults, twins and other extended

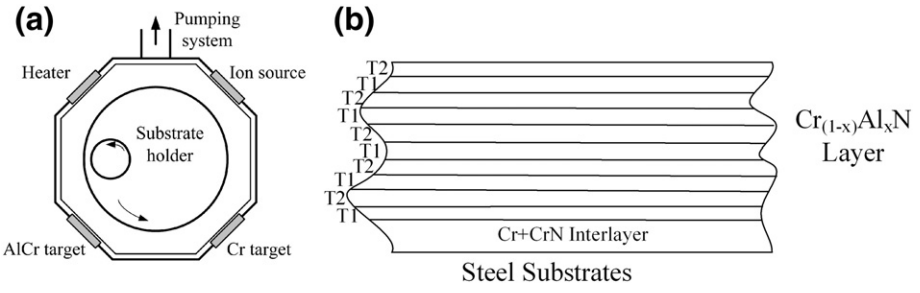

Fig. 1. Schematic diagrams of (a) deposition apparatus and (b) multilayer AlCrN film. Sublayers marked by T1 and T2 correspond to duration of N_2 flow T_1 and T_2 with rates H_1 and H_2, respectively (see Table 1).

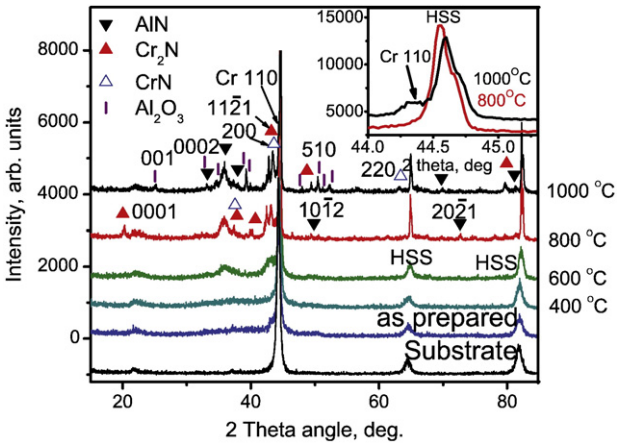

Fig. 2. XRD patterns (θ–2θ scans) of multilayer $Cr_{(1-x)}Al_xN$ films annealed at different temperatures T_{ann} indicated. For easy comparison, the XRD patterns are shifted vertically. The theoretical positions of the crystalline phases observed are indicated by different symbols. Miller indices *hkl* (or *hkil* for hcp phases) for selected reflections are shown. Inset presents the part of the XRD pattern in vicinity of Cr 200 reflection overlapped with high-intensive HSS substrate reflection at an enlarged scale.

imperfections. Additionally, dislocations, vacancies, interstitials, substitution and other defects could cause strain in crystallites leading to reflection profile broadening. Due to a different type of θ-angular dependence, the strain and crystallite size broadening effect could be resolved (see [26], for example). However, for the films under investigation, XRD model with strain present in all crystalline phases was not consistent with experimental data. This means that XRD data precision is insufficient for determination of the strain due to bad intensity statistics of the XRD reflections, or alternatively the absence of strain. Neglecting the strain, the calculation of crystallite size was performed taking into account all measured XRD reflections for the observed individual crystalline phases resulting in high estimated standard deviation (e.s.d.) of the values obtained. Finally, to obtain more precise data, the size of AlN, CrN and Cr_2N crystallites along, respectively, [0001], [100] and [11$\bar{2}$1] crystallographic directions of corresponding lattices based on analysis of most high-intensity non-substrate reflections, namely AlN 0002, CrN 200 and Cr_2N 11$\bar{2}$1, was estimated.

The crystallite size contribution to the reflection profile broadening was calculated using the Scherrer formula [27]:

$$FWHM_{size} = K\cdot\lambda/(D\cdot\cos(\theta_B)), \quad (1)$$

where $FWHM_{size}$ is contribution to FWHM of a reflection due to crystallite size, $K = 0.94$, λ is the wave length of the X-ray radiation used, D is the crystallite size, and θ_B is half of the Bragg angle $2\theta_B$. Taking into account nearly Lorentzian shape of the reflection profiles (for all crystalline phases detected, observed $FWHM/\beta \approx 0.67$, whereas for Lorentzian profiles $FWHM/\beta = 0.637$ [28], where β is the integral breadth of the reflection) and following [26], the instrumental broadening was corrected as

$$FWHM_{corr} = FWHM - FWHM_{instr}. \quad (2)$$

In absence of the strain broadening, there is

$$FWHM_{size} = FWHM_{corr}. \quad (3)$$

The results of crystallite size calculations for different annealing temperatures are summarized in Table 2 together with relative maximum intensities and interplane distances d of the corresponding XRD reflections obtained from the Bragg angles by the Bragg's law. It can be seen that the annealing temperature affects the crystallite size and crystal interplane spacing and XRD reflection intensities as well. The d-spacings of the XRD reflections attributed to different crystalline phases are becoming larger with increased annealing temperature up to 800 °C, reflecting a lattice expansion due to strain relaxation. After annealing at 1000 °C, the d-spacings of the hcp-AlN phase remain constant whereas for hcp-Cr_2N and cubic CrN they shrunk evidencing lattice compression of these crystalline phases most likely due to nitrogen release. The crystallite size along [0001] direction according to AlN 0002 reflection showed a significant increase from 4.0(5) nm at 600 °C to 8.2(3) nm at 1000 °C. At the same time, the crystallites size based on CrN 200 and Cr_2N 11$\bar{2}$1 reflections increased from 13(9) nm and 15(1) nm after 600 °C annealing up to 25(8) nm and 166(35) for $T_{ann} = 1000$ °C, respectively. The diffraction intensity ratio of the XRD reflections of crystalline phases at different annealing temperatures also shown in Table 2 exhibits a sharp increase, which is almost about two or three times larger at 1000 °C than at 600 °C evidencing the crystalline phase content increasing with temperature.

The θ–2θ scan mode used for obtaining the XRD patterns presented above provides structural information from rather large depths nearby the sample surface. The penetration depth τ is defined by the summary incidence and exit path length, in which the intensity I of the X-rays passing through the material is attenuated to $1/e$ of the primary intensity I_0 due to absorption in the material, i.e. about 63% of the diffracted intensity originates from a volume confined by the depth τ below the sample surface. According to $W_{18}Cr_4V$ composition of the HSS steel and known linear absorption coefficients of the composing metals, the absorption coefficient μ_l of the HSS substrate was estimated at 2977(100) cm^{-1}. Taking into account that only AlN and Cr_2N XRD reflections were detected in glancing incidence XRD patterns recorded at small incidence angles ω up to 4° representative for the phase content of the $Cr_{(1-x)}Al_xN$ multilayer (see below), the contribution of Cr and CrN was neglected during estimation of the absorption coefficient of the multilayer. Considering the ratio of integral intensities of the AlN and Cr_2N XRD reflections observed after annealing at 1000 °C, the composition of the $Cr_{(1-x)}Al_xN$ multilayer was estimated at 85(4) vol.% AlN and 14(4) vol.% Cr_2N, which is in a reasonable agreement with the nominal content of Al in the target (about 70 at.%) during the sample preparation. From the obtained composition of the $Cr_{(1-x)}Al_xN$ multilayer and linear absorption coefficients of the AlN ($\mu_l = 112.9$ cm^{-1}) and Cr_2N ($\mu_l = 1557.8$ cm^{-1}) calculated from known structure models [20,21], the absorption coefficient μ_l of the $Cr_{(1-x)}Al_xN$ multilayer was estimated at 328(70) cm^{-1}. Following the procedure described in [29] and taking into account different absorption coefficients of the HSS substrate and covering $Cr_{(1-x)}Al_xN$ multi-layer with the thickness of about 2 μm, the penetration depth τ in case of θ–2θ scan mode was estimated to vary between 2106(70) nm and 3361(70) nm at $2\theta = 20°$ and 85°, respectively. Thus, during the θ–2θ scanning, the X-rays penetrate through the film into the underlying

Table 2
Interplanar d-spacing and crystallite size D corresponding to indicated reflections of the crystalline phases formed in $Cr_{(1-x)}Al_xN$ films at different annealing temperatures T_{ann}. Relative change of the maximum reflection intensity I_{max}/I_{max} (600 °C) is indicated as well. The standard uncertainties are shown in brackets.

T_{ann}, °C	d, nm	D, nm	I_{max}/I_{max} (600 °C), %
AlN 0002			
600	0.2495(7)	4.0(5)	100
800	0.2505(3)	6.6(3)	146(8)
1000	0.2505(3)	8.2(3)	189(9)
Cr_2N 11$\bar{2}$1			
600	0.2126(2)	15(1)	100
800	0.2128(1)	32(2)	162(8)
1000	0.21123(5)	166(35)	271(10)
CrN 200			
600	0.2089(2)	12.7(9)	100
800	0.20943(9)	24.9(8)	192(8)
1000	0.20823(9)	25.1(8)	243(9)

substrate material. As a result, the XRD reflections of the film and of the substrate overlap and the signal-to-background noise ratio for XRD reflections of the film becomes low.

In order to obtain more detailed information, the glancing incidence XRD (GIXRD) experiments were carried out at glancing angles ω of 2°, 3° and 6° (Fig. 3) corresponding, respectively, to penetration depths τ of 1003(110) nm, 1460(100) nm and 2107(70) nm for the 2θ range of 30° to 50° according to calculations described above. In Fig. 3(a), at glancing incidence angle ω of 2° ($\tau = 1003(110)$ nm), for the as-deposited and 400 °C-annealed films no non-substrate XRD reflections are present. A lot of CrN and Cr_2N reflections in the standard θ–2θ XRD patterns of the 800 °C annealed sample (Fig. 2) represent deep layers of the film and substrate (τ of about 2700 nm). Increasing the annealing temperature to 800 °C resulted in an exclusive formation of hcp-AlN 0002 and hcp-Cr_2N $11\bar{2}1$ reflections in the $\omega = 2°$ GIXRD patterns evidencing the formation of only hcp AlN and Cr_2N crystalline phases at 1000 nm depths in the $Cr_{(1-x)}Al_xN$ film. When the glancing incidence angle ω was increased to 3° (τ of about 1460 nm) and 6° (τ of about 2100 nm), the corresponding GIXRD patterns also didn't show any non-substrate reflections formation for low annealing temperatures up to 400 °C. However, in comparison with $\omega = 2°$ GIXRD patterns, the Al 0002, Cr_2N $11\bar{2}1$ and HSS substrate XRD reflections became stronger and narrower for the 600 °C and 800 °C annealed samples (Fig. 3(b) and (c)), especially for the HSS steel substrate diffraction reflections in agreement with increasing scattering volume of the multilayer and the substrate materials due to increasing penetration depth and higher formation of the crystallites of corresponding phases at larger depths. As a result of increasing the film scattering volume, weak Cr_2N 0002 reflection was detected for the 800 °C annealed sample (Fig. 3(b) and (c)). At the same time, compared with $\omega = 2°$ GIXRD (Fig. 3(a)) and θ–2θ XRD (Fig. 2) patterns, hcp-Cr_2N $11\bar{2}1$ and HSS substrate overlapped reflections got separated and their maximum intensities remain comparable because of increased scattering volume of the film material in GIXRD experiment due to increased area of the film surface illuminated by X-rays.

More detailed evolution of the GIXRD patterns of the samples after annealing at 600 °C and 800 °C with variation of the glancing incidence angle ω is illustrated in Fig. 4(a) and (b), respectively, supporting

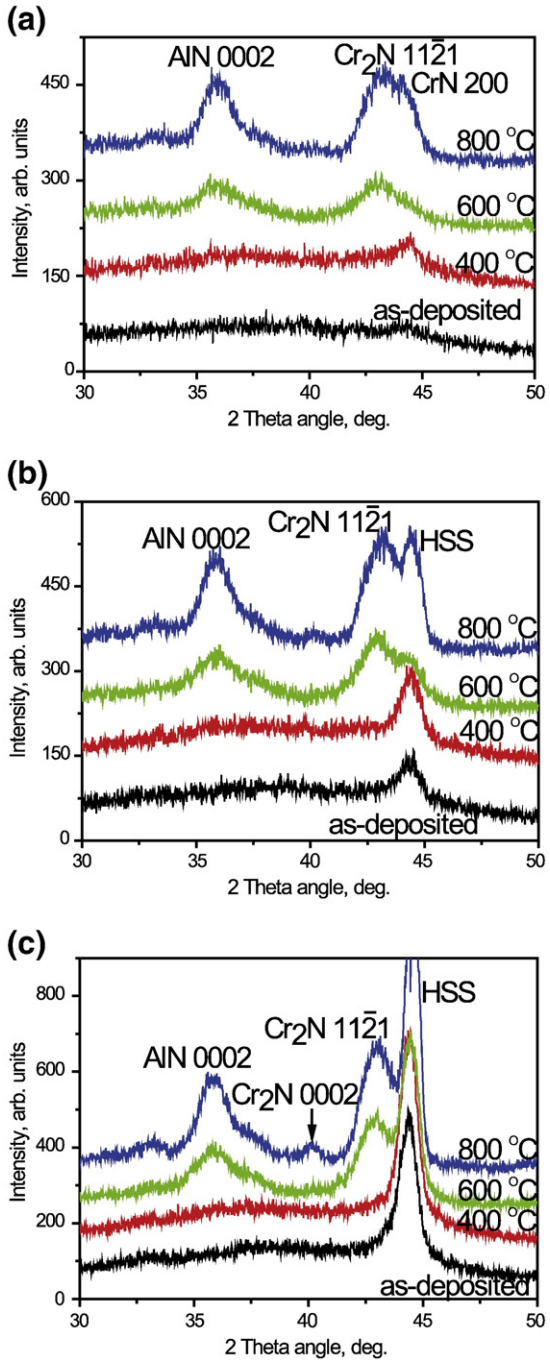

Fig. 3. GIXRD patterns (2θ scans) of multilayer $Cr_{(1-x)}Al_xN$ films obtained at different glancing incidence angles ω: (a) 2° (penetration depth $\tau = 1003(110)$ nm), (b) 3° ($\tau = 1460(100)$ nm), (c) 6° ($\tau = 2107(70)$ nm). For easy comparison, the GIXRD patterns are shifted vertically.

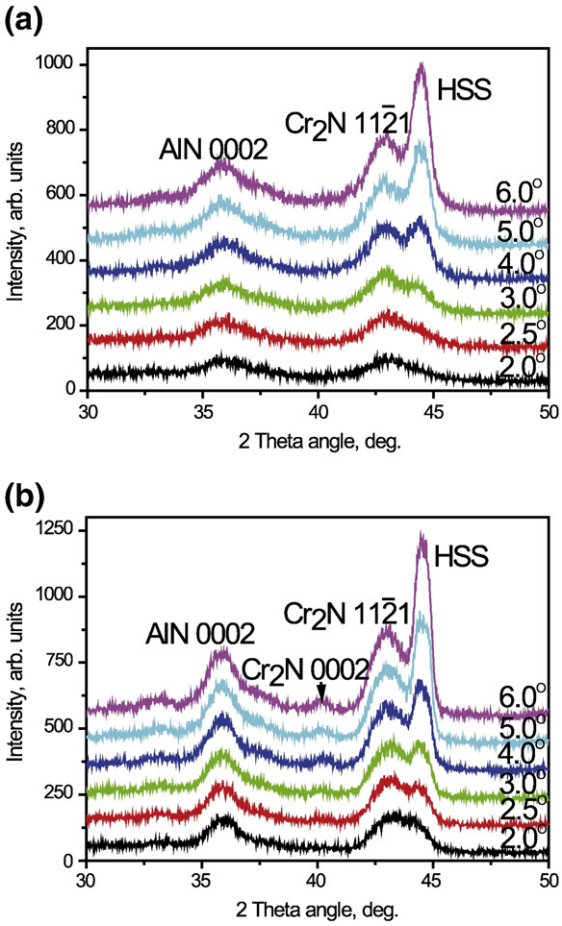

Fig. 4. GIXRD patterns of multilayer $Cr_{(1-x)}Al_xN$ films with different glancing incidence angles ($\omega = 2°, 2.5°, 3°, 4°, 5°$ and 6° corresponding to penetration depths τ of 1003(110) nm, 1235(110) nm, 1460(100) nm, 1887(120) nm, 2032(70) nm and 2107(70) nm, respectively) after annealing at (a) 600 °C and (b) 800 °C.

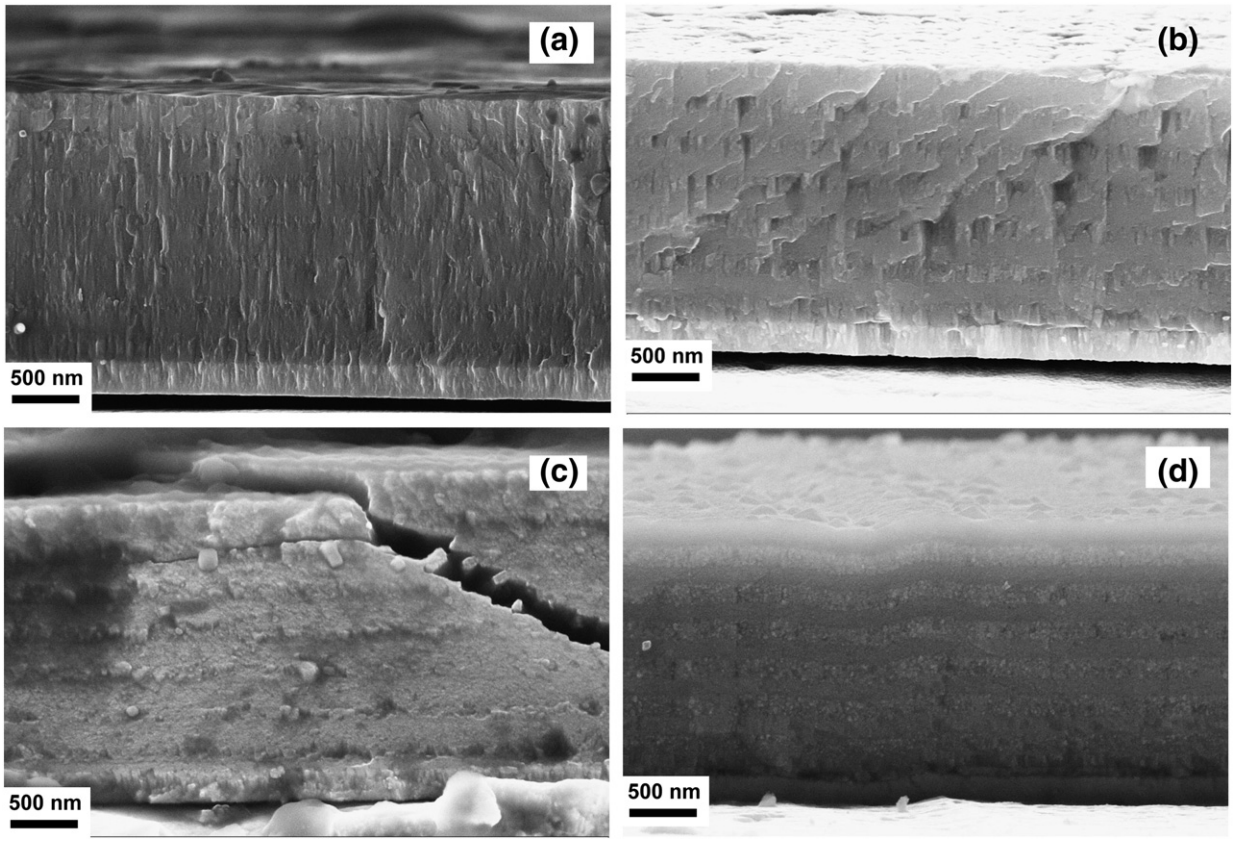

Fig. 5. Cross-sectional SEM images of $Cr_{(1-x)}Al_xN$ multilayer films after different annealing temperatures: (a) as-deposited, (b) 400 °C, (c) 600 °C, (d) 800 °C.

discussed observations. Note that the GIXRD patterns recorded at glancing angles $\omega = 2°$ and 2.5° (penetration depths $\tau = 1003(110)$ nm and 1235(110) nm, respectively) are similar starting to change (see above for the changes) at $\omega = 3°$ ($\tau = 1460(100)$ nm) refining the 1460 nm depth value where the enhanced formation of the AlN and Cr_2N crystallites is observed resulting in an increase of the intensity of corresponding diffraction reflections.

Annealing effects on the interfacial microstructure were investigated by means of cross-sectional microscopy. Cross-sectional SEM images, including the Cr interlayer/substrate interface of the multilayer $Cr_{(1-x)}Al_xN$ films are shown in Fig. 5. The coating is quite dense with no apparent pores or inclusions present. Several studies show that a metal interlayer, 0.5 μm to 1.5 μm thick helps to accommodate coating residual stresses and allows for a thicker coating to be deposited, with significant improvements in toughness, adhesion, and impact resistance [30–34]. From Fig. 5(a) it is seen that the coating and Cr interlayer in the as-deposited sample has typical columnar grains of about 50–150 nm in width, which corresponds to the T zone according to the Thornton's structure zone model [35]. At the Cr interlayer and multilayer film interface some of the Cr columnar structures are blocked by the interface, while some $Cr_{(1-x)}Al_xN$ grains re-nucleate at the top interface. Interfaces of individual layers with different nitrogen content can also be seen clearly in Fig. 5(a) for the as-deposited sample because of different contrast. Fig. 5(b) is a cross-sectional SEM image of the 400 °C annealed samples, which exhibits a transition from columnar to equiaxed structure with a clearly defined interface. When the annealing temperature increased to 600 °C, both coating and the Cr interlayer had equiaxed grains (Fig. 5(c)) with larger crystal size at the interface than elsewhere. Fig. 5(d) shows cross-sectional SEM images after annealing at 800 °C, where interfaces become better defined. Different layers are separated by clearly defined interfaces because of diffusion and crystal growth. Diffusion may take place in every layer and interface, but the energy barrier for interfacial diffusion is much higher than in layers, so diffusion is much easier in the layers and more clear interfaces are seen with higher annealing temperature.

Hardness and elastic modulus data obtained from $Cr_{(1-x)}Al_xN$ films annealed at different conditions are presented in Fig. 6. The nanoindentation depth was kept below 10% of the coating thickness to avoid the substrate effects. It can be seen that annealing treatment can significantly change both hardness and elastic modulus. Hardness of the as-deposited amorphous $Cr_{(1-x)}Al_xN$ film is 22.6 GPa. After annealing at 400 °C for 1 h, hardness increased to 26.7 GPa, and then did not change much with the annealing temperature increasing to

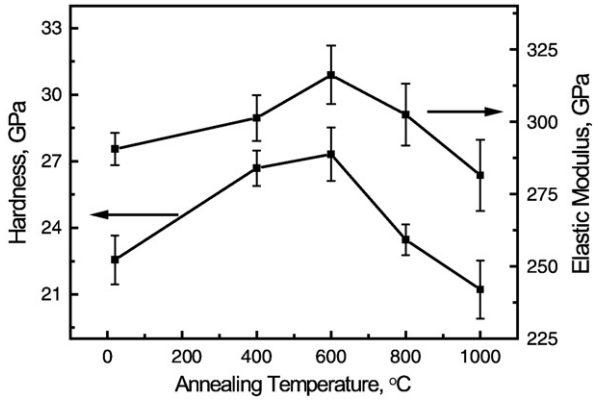

Fig. 6. Hardness and elastic modulus of multilayer $Cr_{(1-x)}Al_xN$ films versus annealing temperature.

600 °C. In contrast, when the film was annealed at 800 °C for 1 h, its hardness decreased to 23.5 GPa due to the growth of crystalline grains (seen SEM image presented in Fig. 5(c)). When annealing temperature was increased to 1000 °C, the hardness decreased again to 21.2 GPa due to the larger crystalline grains. The elastic modulus of the films shows similar trends as the hardness. Comparison with XRD results reveals a similar correlation of the mechanical properties of the films and their microstructure. Based on the XRD analysis, as-deposited films are mostly amorphous, so the hardness and elastic modulus are lower.

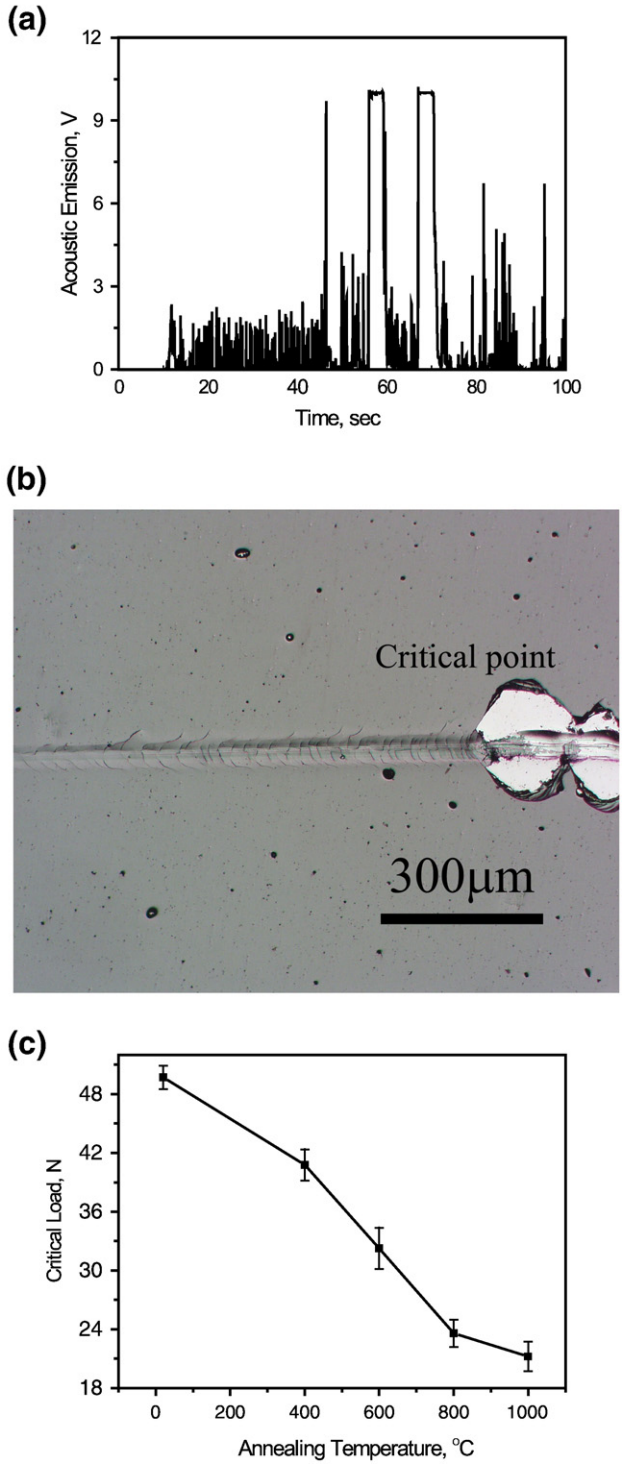

Fig. 7. (a) Acoustic emission signal used for detecting a critical point of film failure during the scratch test; (b) scratch scar optical image; (c) adhesion (critical normal force) versus annealing temperature.

When the temperature T_{ann} is increased to 400 °C, evidently there are new AlN and Cr_2N crystalline phases that started to form but were not detected by XRD probably due to their small scattering volume. As a result, the hardness and elastic modulus show a slight increase observed in Fig. 6. Probably, $T_{ann} = 600$ °C is an optimal annealing temperature resulting in optimal crystallite sizes (see Table 2) and in the maximum hardness and elastic modulus values. After annealing at 800 °C and 1000 °C, the crystallite size became much larger and the Cr_2N phase started to transform to metallic Cr and non-dense surface aluminum oxide Al_2O_3 started to form, so the hardness and elastic modulus became smaller.

Adhesion is an important property of thin films and coatings. Scratch test is a popular method to characterize the adhesion between the film and the substrate, although it is difficult to define the critical fracture load with this method. We utilized acoustic emission to determine the critical normal fracture load. Fig. 7(a) shows the acoustic emission signal when a scratch test was carried out. From this figure the critical normal load can be easily identified with the changing lateral force and increasing acoustic emission signal. Fig. 7(b) shows the optical image of a scratch scar at the critical point, which corresponds to Fig. 7(a). Fig. 7(c) shows the critical normal load of the interfacial failures at different annealing temperatures. With increasing annealing temperature the critical normal load decreased from 49.7 N for the as-deposited film to 21.2 N for the film annealed at 1000 °C, which may be caused by high interfacial stress between films and substrate due to the difference in their thermal expansion coefficients.

The above experiments show that the film microstructure and diffusion in film layers can be investigated by XRD and SEM. Films' atomic structure changed from amorphous to crystalline with annealing temperature accompanied by different phase transformations. Mechanical properties changes correspond to the microstructure changes. The hardness and elastic modulus show a slight increase with annealing temperature, but they show different trend when the annealing temperature is higher than 600 °C due to increasing crystallite size and crystalline phase transformations. Adhesion shows a decreasing trend with increasing annealing temperature because of stress levels attributed to different thermal expansion coefficients of substrate and films.

4. Conclusions

Multilayer $Cr_{(1-x)}Al_xN$ films were deposited on high-speed steel substrates by medium frequency magnetron sputtering with a total thickness of 2 μm. XRD showed that the films mainly consist of hcp-AlN and hcp-Cr_2N phases. hcp-Cr_2N transformed into bcc-Cr and N_2 with higher annealing temperature. The grain size of as-deposited multilayer films is fine, and increases significantly with annealing temperature. Cross-sectional SEM images showed that Cr interlayer and $Cr_{(1-x)}Al_xN$ films have typical columnar structure. Films developed equiaxed grains structure, and interfaces became better defined with higher annealing temperature. The hardness and elastic modulus of multilayer AlCrN films annealed at different temperatures were measured by nanoindentation. Hardness decreased with higher annealing temperature due to grain growth and higher content of the crystalline phases. Higher annealing temperature also decreased $Cr_{(1-x)}Al_xN$ multilayer film adhesion.

Acknowledgements

This work was supported by the China State Key Lab of Advanced Metals and Materials and the National Science Foundation of China (51001013).

References

[1] R. Franz, J. Neidhardt, B. Sartory, R. Tessadri, C. Mitterer, Thin Solid Films 516 (2008) 6151.
[2] Y.C. Chim, X.Z. Ding, X.T. Zeng, S. Zhang, Thin Solid Films 517 (2009) 4845.

[3] H. Willmann, M. Beckers, J. Birch, P.H. Mayrhofer, C. Mitterer, L. Hultman, Thin Solid Films 517 (2008) 598.
[4] J.L. Mo, M.H. Zhu, Tribol. Int. 41 (2008) 1161.
[5] Jose L. Endrino, Volker Derflinger, Surf. Coat. Technol. 200 (2005) 988.
[6] H. Willmann, P.H. Mayrhofer, P.O.A. Persson, A.E. Reiter, L. Hultman, C. Mitterer, Scr. Mater. 54 (2006) 1847.
[7] E. Le Bourhis, P. Goudeau, M.H. Staia, E. Carrasquero, E.S. Puchi-Cabrera, Surf. Coat. Technol. 203 (2009) 2961.
[8] M. Holzherr, M. Falza, T. Schmidt, Surf. Coat. Technol. 203 (2008) 505.
[9] G.S. Fox-Rabinovich, K. Yamomoto, S.C. Veldhuis, A.I. Kovalev, G.K. Dosbaeva, Surf. Coat. Technol. 200 (2005) 1804.
[10] A.E. Reiter, V.H. Derflinger, B. Hanselmann, T. Bachmann, B. Sartory, Surf. Coat. Technol. 200 (2005) 2114.
[11] R. Hoy, W.G. Sloof, G.C.A.M. Janssen, Surf. Coat. Technol. 179 (2004) 215.
[12] J.L. Endrino, G.S. Rox-Rabinovich, C. Gey, Surf. Coat. Technol. 200 (2006) 6840.
[13] R. Franz, J. Neidhardt, B. Sartory, R. Kaindl, R. Tessadri, P. Polcik, V.H. Derflinger, C. Mitterer, Tribol. Lett. 23 (2006) 101.
[14] G.S. Kim, S.Y. Lee, Surf. Coat. Technol. 201 (2006) 4361.
[15] J.L. Mo, M.H. Zhu, Wear 267 (2009) 874.
[16] S.M. Lee, H.M. Chow, F.Y. Huang, B.H. Yan, Int. J. Mach. Tool. Manuf. 49 (2009) 81.
[17] Programm ANALYZE, Rayflex Version 2.285, Rich. Seifert & Co, 2000.
[18] Powder diffraction file (PDF), Release 2001, International Centre for Diffraction Data, 2001.
[19] Inorganic Crystal Structure Database (ICSD), Version 1.4.2, Release 2007, National Institute of Standards and Technology (NIST) and Fachinformationszentrum Karlsruhe (FIZ), Karlsruhe, 2007.
[20] G.A. Jeffrey, G.S. Parry, R.L. Mozzi, J. Chem. Phys. 23 (1955) 406.
[21] S.J. Kim, T. Marquart, H.F. Franzen, J. Less-Common Met. 158 (1990) L9.
[22] M. Nasr Eddine, E.F. Bertaut, M. Roubin, J. Paris, Acta Crystallogr. B 33 (1977) 3010.
[23] H.E. Swanson, N.T. Gilfrich, G.M. Ugrinic, Natl. Bur. Stand. U. S. 539 (1955) 5.
[24] Gmelins Handbuch der anorganischen Chemie, Verlag Chemie, Wenheim, 1962, p. 160.
[25] E. Husson, Y. Repelin, Eur. J. Sol. State Inor. 33 (1996) 1223.
[26] B.E. Warren, X-ray Diffraction, Courier Dover Publ, New York NY, 1990.
[27] R.A. Young, A. Sakthivel, T.S. Moss, C.O. Paiva-Santos, J. Appl. Cryst. 28 (1995) 366.
[28] J. Langford, Accuracy in Powder Diffraction, Natl. Bur. Stand. Spec. Publ., No 5137, 1980.
[29] A. Kumar, U. Welzel, E.J. Mittemeijer, J. Appl. Crystallogr. 39 (2006) 633.
[30] X. Pang, K. Gao, H. Yang, L. Qiao, Y. Wang, A.A. Volinsky, Adv. Eng. Mater. 9 (2007) 594.
[31] G.S. Kim, S.Y. Lee, J.H. Hahn, B.Y. Lee, J.G. Han, J.H. Lee, S.Y. Lee, Surf. Coat. Technol. 171 (2003) 83.
[32] X. Pang, K. Gao, F. Luo, H. Yang, L. Qiao, Y. Wang, A.A. Volinsky, Thin Solid Films 516 (2008) 4685.
[33] X. Pang, K. Gao, A.A. Volinsky, J. Mater. Res. 22 (2007) 3531.
[34] X. Pang, K. Gao, F. Luo, Y. Emirov, A.A. Levin, A.A. Volinsky, Thin Solid Films 517 (2009) 1922.
[35] J.A. Thornton, Annu. Rev. Mater. Sci. 7 (1977) 239.